



OPEN Unified total body CT image with multiple organ specific windowings: validating improved diagnostic accuracy and speed in trauma cases

Naoki Okada^{1,5}✉, Shusuke Inoue², Chang Liu¹, Sho Mitarai¹, Shinichi Nakagawa³, Yohsuke Matsuzawa⁴, Satoshi Fujimi⁵, Goshiro Yamamoto¹ & Tomohiro Kuroda¹

Total-body CT scans are useful in saving trauma patients; however, interpreting numerous images with varied window settings slows injury detection. We developed an algorithm for “unified total-body CT image with multiple organ-specific windowings (Uni-CT)”, and assessing its impact on physician accuracy and speed in trauma CT interpretation. From November 7, 2008, to June 19, 2020, 40 cases of total-body CT images for blunt trauma with multiple injuries, were collected from the emergency department of Osaka General Medical Center and randomly divided into two groups. In half of the cases, the Uni-CT algorithm using semantic segmentation assigned visibility-friendly window settings to each organ. Four physicians with varying levels of experience interpreted 20 cases using the algorithm and 20 cases in conventional settings. The performance was analyzed based on the accuracy, sensitivity, specificity of the target findings, and diagnosis speed. In the proposal and conventional groups, patients had an average of 2.6 and 2.5 targeting findings, mean ages of 51.8 and 57.7 years, and male proportions of 60% and 45%, respectively. The agreement rate for physicians’ diagnoses was $\kappa = 0.70$. Average accuracy, sensitivity, and specificity of target findings were 84.8%, 74.3%, 96.9% and 85.5%, 81.2%, 91.5%, respectively, with no significant differences. Diagnostic speed per case averaged 71.9 and 110.4 s in each group ($p < 0.05$). The Uni-CT algorithm improved the diagnostic speed of total-body CT for trauma, maintaining accuracy comparable to that of conventional methods.

Keywords Diagnostic imaging, Deep learning model, Automated windowing, Trauma

The annual global incidence of trauma patients exceeds 100 million, with a mortality rate surpassing 10%^{1–3}, emphasizing the critical nature of trauma care. The use of total-body computed tomography (CT) is beneficial in the evaluation of patients with severe trauma^{4–6}. Advances in CT technology have led to faster imaging processes and have accelerated these trends⁷. However, lengthy interpretation times for total-body CT images delay intervention, which can result in poorer patient outcomes⁸. Consequently, reducing the time required for CT interpretation has become a crucial challenge in improving patient outcomes.

Hence, exploring interpretation protocols of total-body CT images in trauma have ensued^{9,10}. A notable approach is the Focused Assessment with CT for Trauma (FACT)¹¹, aiming to interpret total body CT findings of trauma within 2–3 min, focusing on observations crucial for urgent treatment decisions. The FACT includes the following fatal findings: extensive intracranial hematomas, aortic injuries, mediastinal hematomas, extensive lung contusions, hemo/pneumothorax, cardiac tamponade, hematomas in the bladder-rectal space, pelvic and vertebral fractures, retroperitoneal hematomas, and parenchymal organ injuries. This approach allows rapid intervention in potentially fatal injuries. However, similar to traditional interpretation methods, this requires adjusting window settings for each organ of interest, often requiring multiple references to the same slice image. For example, under soft-tissue conditions, the aortic arch and mediastinal hematoma are first assessed. The

¹Graduate School of Informatics, Kyoto University, Yoshida-honmachi, Sakyo-ku, Kyoto-shi, Kyoto 606-8501, Japan. ²fcuro inc, Osaka-shi, Osaka, Japan. ³Uji Tokushukai Hospital, Uji-shi, Kyoto, Japan. ⁴Osaka Metropolitan University, Osaka-shi, Osaka, Japan. ⁵Osaka General Medical Center, Osaka-shi, Osaka, Japan. ✉email: naoki_okada@kuhp.kyoto-u.ac.jp

settings are subsequently changed to lung conditions to evaluate extensive lung contusions or pneumothorax. The need to constantly switch settings for optimal organ visualization is a current limitation for the efficient interpretation of CT images^{12,13}.

Some studies have explored windowing methods aiming to simultaneously evaluate multiple organs^{14–18}. For example, window blending overlays images of lung, soft tissue, and bone window settings to evaluate chest trauma in a single series of images. However, these methods use superimposition techniques, inhibiting the physician's ability to evaluate each organ by obscuring the distinct characteristics of each windowings^{14,19}. To address this, we introduced a “unified CT image using organ-specific windowing (Uni-CT)” algorithm to automatically generate a single series of total-body CT images concatenating multiple images of segmented organs with organ-specific window settings. Our algorithm utilizes semantic segmentation models to extract organs, processes their window settings, and then concatenates these organ-specific window settings images without superimposing multiple window settings images. Concatenated images do not lose distinct characteristics of each organ-specific window setting. This allows for the evaluation of total -body from a single series of images without any manual manipulation, enhancing the efficiency of CT interpretation. Our study also validates the effectiveness of this algorithm in the trauma CT interpretation of physicians.

Methods

Ethics approval

This study was approved by the Clinical Medicine Ethics Committee at Osaka General Medical Center (IRB:2021-070). The requirement for written informed consent was waived because of the retrospective nature and minimal risk to the study participants. This study was conducted in accordance with the principles of the Declaration of Helsinki. A summary of the study was posted at all participating institutions. This study was registered in the Japan Registry of Clinical Trials (jRCT1050230166).

Image datasets

CT images of trauma cases were collected between November 7, 2008, and June 19, 2020, at Osaka General Medical Center. The inclusion criteria were blunt trauma patients who underwent enhanced total-body CT scanning, exhibiting multiple findings such as aortic injury, mediastinal hematoma, extensive lung contusion, pneumothorax, cardiac tamponade, hematoma in the bladder-rectal space, pelvic and vertebral fractures, retroperitoneal hematoma, and parenchymal organ injury. Images with severe artifacts, missing data, or poor depiction were excluded. In total, 40 cases were anonymized and collected retrospectively. The images were captured in DICOM format using three different CT machines (Aquilion 64, Aquilion CX, and Aquilion PRIME; Canon Medical Systems Corporation, Otawara, Japan). Imaging commenced 90 s after contrast agent administration, using axial slice images with a thickness of 5 mm from neck to pelvis. The 40 cases were arranged chronologically and randomly divided into two groups using the Fisher-Yates shuffle method²⁰: the first 20 cases formed the proposal group, and the remaining 20 constituted the conventional group.

Annotation

Annotations were based on diagnoses made by board-certified radiologists with over 10 years of clinical experience. Findings on aortic injury, mediastinal hematoma, extensive lung contusion, pneumo/hemothorax, cardiac tamponade, intra abdominal hematoma (usually a hematoma in the bladder-rectal space), pelvic and vertebral fractures, retroperitoneal hematoma, and parenchymal organ injury were extracted. These findings were categorized into five groups based on the FACT protocol for rapid total-body CT image diagnosis in trauma¹¹. Aortic injury and mediastinal hematoma were categorized as group A; extensive lung contusion, pneumo/hemothorax, and cardiac tamponade as group B; intra abdominal hematoma as group C; pelvic/vertebral fractures and retroperitoneal hematoma as group D; and parenchymal organ injury as group E.

Algorithm structure

The image-generation algorithm was composed of three steps. In the first step, anatomical structures are extracted from total-body CT images using a semantic segmentation model²¹. Second, the optimal window settings for each extracted anatomical structure were dynamically calculated and applied to window processing. For other regions that did not belong to the extracted structures, a fixed soft-tissue window setting was applied. In the last step, all organ-specific window-setting images were concatenated into a single series of images (Fig. 1).

Extraction of anatomical structures

Initially, CT data in DICOM format were converted to NifTI format using the dicom2nifti library (version 2.4.6). Subsequently, the TotalSegmentator library (version 1.5.6) was used to detect anatomical structures from the CT images²¹. This library provides a group of deep learning models for semantic segmentation of 104 different anatomical structures from CT images. Lower-resolution models were used to detect anatomical structures in the algorithm. From the initially detected 104 classes, excluding those related to the head, blood vessels, and muscles, we consolidated them into 23 classes: trachea, lungs, heart, esophagus, stomach, duodenum, small intestine, colon, liver, gallbladder, pancreas, spleen, adrenal glands, kidneys, ureters, vertebrae, clavicle, ribs, scapula, humerus, ilium, sacrum, and femur²² (Table 1).

The segmentation information for these 23 classes of anatomical structures was output as binary data, where pixels corresponding to each class were assigned a value of ‘1,’ and all other regions were assigned a value of ‘0.’ To smooth the boundaries of each anatomical structure, we implemented anti-aliasing processing²³ using the resize function with linear interpolation from the OpenCV library (version 4.6.0.66). The segmentation information was first reduced in size by one-fourth in both dimensions using area averaging, and gradually

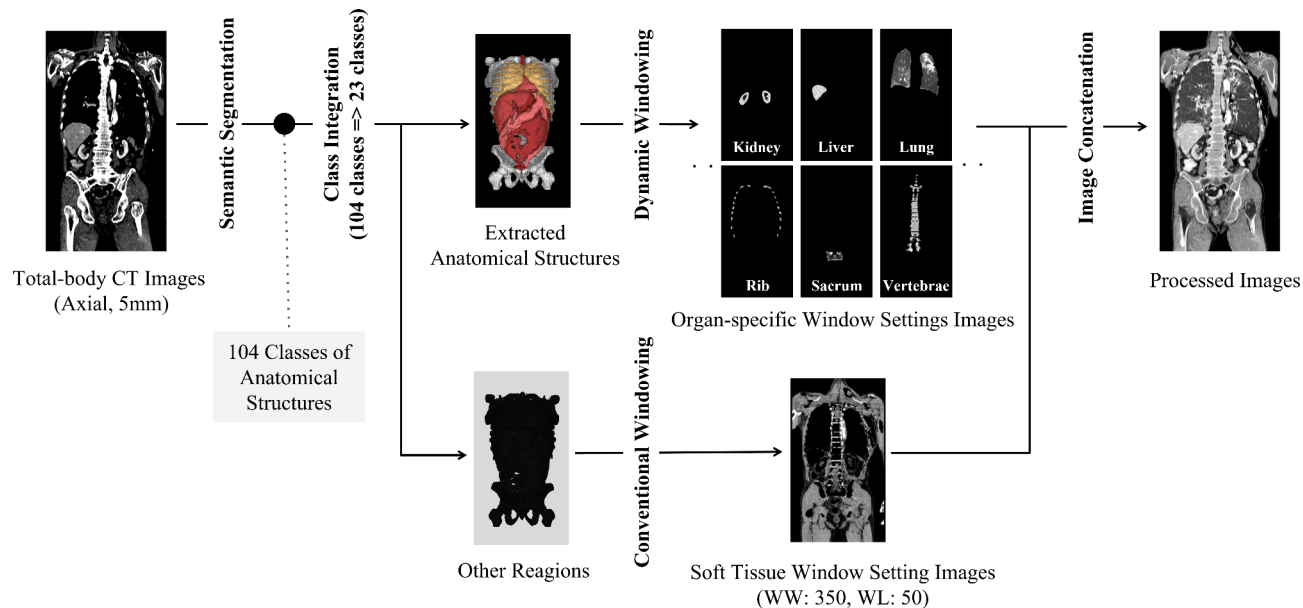


Fig. 1. Overview of the algorithm. The augmented visualization windowing algorithm is composed of three steps. First, anatomical structures were extracted using a semantic segmentation model, followed by the calculation of organ-specific window settings for each anatomical structure. In the final step, all the images were concatenated.

| Consolidated class | Original class of TotalSegmentator |
|--------------------|--|
| adrenal | adrenal_gland_left, adrenal_gland_right |
| clavicula | clavicula_left, clavicula_right |
| colon | colon |
| duodenum | duodenum |
| esophagus | esophagus |
| femur | femur_left, femur_right |
| gallbladder | gallbladder |
| heart | heart_atrium_left, heart_atrium_right, heart_myocardium, heart_ventricle_left, heart_ventricle_right |
| hip | hip_left, hip_right |
| humerus | humerus_left, humerus_right |
| kidney | kidney_left, kidney_right |
| liver | liver |
| lung | lung_lower_lobe_left, lung_lower_lobe_right, lung_middle_lobe_right, lung_upper_lobe_left, lung_upper_lobe_right |
| pancreas | pancreas |
| rib | rib_left_1, rib_left_2, rib_left_3, rib_left_4, rib_left_5, rib_left_6, rib_left_7, rib_left_8, rib_left_9, rib_left_10, rib_left_11, rib_left_12, rib_right_1, rib_right_2, rib_right_3, rib_right_4, rib_right_5, rib_right_6, rib_right_7, rib_right_8, rib_right_9, rib_right_10, rib_right_11, rib_right_12 |
| sacrum | sacrum |
| scapula | scapula_left, scapula_right |
| small_bowel | small_bowel |
| spleen | spleen |
| stomach | stomach |
| trachea | trachea |
| urinary_bladder | urinary_bladder |
| vertebrae | vertebrae_c1, vertebrae_c2, vertebrae_c3, vertebrae_c4, vertebrae_c5, vertebrae_c6, vertebrae_c7, vertebrae_l1, vertebrae_l2, vertebrae_l3, vertebrae_l4, vertebrae_l5, vertebrae_t1, vertebrae_t2, vertebrae_t3, vertebrae_t4, vertebrae_t5, vertebrae_t6, vertebrae_t7, vertebrae_t8, vertebrae_t9, vertebrae_t10, vertebrae_t11, vertebrae_t12 |
| - (other regions) | aorta, autochthon_left, autochthon_right, gluteus_maximus_left, gluteus_maximus_right, gluteus_medius_left, gluteus_medius_right, gluteus_minimus_left, gluteus_minimus_right, iliac_artery_left, iliac_artery_right, iliac_vena_left, iliac_vena_right, iliopsoas_left, iliopsoas_right, inferior_vena_cava, portal_vein_and_splenic_vein, pulmonary_artery |

Table 1. Consolidation of Classes The TotalSegmentator output classes are compiled from the original classes in the right row to the left column.

enlarged to the original size in stages of 3/2, 5/3, and 8/5. This process involves converting pixel areas with values greater than '0' back to '1,' thereby reverting them to binary data. Pixels that did not belong to any of the 23 classes after processing were defined as other regions.

Dynamic windowing processing

The anatomical structures of the 23 classes obtained were subjected to dynamic windowing processing and optimized for each organ. Using the NumPy library (version 1.23.3), the percentile scores were selected as the upper and lower limits for each class based on the distribution of their CT values. The difference between the upper and lower CT values was calculated as the window width (WW) and the average of these values was determined as the window level (WL)²⁴. For the other regions, fixed values commonly used for soft tissue conditions (WW = 350 and WL = 50) were applied²⁵. Based on these calculations, window processing was conducted for each class, and the results were integrated to generate 8-bit grayscale images.

Interpretation test using algorithm-processed images

The percentile settings for dynamic window processing were determined by classifying the 23 anatomical classes into three categories: SOFT_TISSUE, BONE, and LUNG (Table 2). The settings were based on the percentile scores for each category with the lower limit as the x-percentile and the upper limit as the y-percentile. For SOFT_TISSUE, the settings were (x, y) = (2.5, 97.5); for BONE, (x, y) = (0, 97.5); and for LUNG, (x, y) = (0, 90). These settings were determined based on the noise characteristics of the CT data used and may require adjustments depending on the utilization environment.

Interpretation tests were conducted on 20 cases each from the proposal and conventional groups. Four physicians with varying years of experience and specialties (a 20-year board-certificated radiologist, a 27-year board-certificated emergency physician, a 3rd-year emergency physician, and a 4th-year internist) were selected for the tests. These physicians had no direct clinical involvement with the patients and were provided only with axial slice images of 5 mm thickness from total-body CT scans of trauma patients, without additional clinical information. They diagnosed the presence or absence of five groups of findings: aortic injury and mediastinal hematoma were categorized as group A; extensive lung contusion, pneumo/hemothorax, and cardiac tamponade as group B; intra abdominal hematoma as group C; pelvic/vertebral fractures and retroperitoneal hematoma as group D; and parenchymal organ injury as group E.

Additionally, the interpretation time for each case was recorded.

Statistical analyses

All analyses were performed using R version 4.3.2. The accuracy, sensitivity, and specificity were calculated for each case, and the average values were computed for all cases. Fleiss' kappa values²⁶ were determined to evaluate the level of agreement among the diagnoses of the four physicians. One-sided two-sample t-tests²⁷ were performed to compare the interpretation times with and without the assistance of the algorithm. Additionally, 95% confidence intervals (CI) were obtained for these analyses.

Results

Dataset characteristics

Patients in the proposal group were in the range of 10–90 years old (average: 51.8, standard deviation: 25.3), whereas those in the conventional group were in the range of 19–83 years old (average: 57.7, standard deviation: 18.7). The female percentages in proposal and conventional groups were 40.0% and 55.0%, respectively. The average number of positive findings per case was 2.6 for the proposal group and 2.5 for the conventional group. Table 3 presents a detailed breakdown of positive findings in each group.

Features of total-body CT algorithm-processed images

Applying the Uni-CT algorithm demonstrated the potential for rapidly identifying critical injuries in total-body CT for trauma without the need to switch window settings between the lung, soft tissue, and bone (The processing time of the algorithm is in Supplementary Sect. 1). Nine representative axial images highlight this effect (Fig. 2). The processed images of the chest (Fig. 2A, B, C) show optimized ribs, vertebrae, lungs, and cardiovascular structures, allowing simultaneous detection of rib fractures, vertebral fractures, pneumothorax, and major vascular injuries. The images of the upper abdomen (Fig. 2D, E, F) show optimized ribs, lungs, liver, gallbladder, duodenum, pancreas, spleen, vertebrae, stomach, intestines, and major blood vessels, enabling simultaneous detection of rib fractures, vertebral fractures, major vascular injuries, and injuries to various

| Category | Percentile cutoff | | Classes |
|-------------|-------------------|-------|--|
| | Lower | Upper | |
| Soft Tissue | 2.5 | 97.5 | adrenal, colon, duodenum, esophagus, gallbladder, heart, kidney, liver, pancreas, small_bowel, spleen, stomach, trachea, urinary |
| Bone | 0 | 97.5 | clavicula, femur, hip, humerus, rib, sacrum, scapula, vertebrae |
| Lung | 0 | 90 | lung |

Table 2. Percentile Settings for Each Anatomical Class.

| | Proposal | Conventional |
|------------------|-----------------|-----------------|
| No. of Patients | | |
| Male | 12 | 9 |
| Female | 8 | 11 |
| Age \pm SD (y) | 51.8 \pm 25.3 | 57.7 \pm 18.7 |
| Min (y) | 10 | 19 |
| Max (y) | 90 | 83 |
| No. of Labels | | |
| Label A | 2 | 1 |
| Label B | 18 | 19 |
| Label C | 1 | 3 |
| Label D | 20 | 20 |
| Label E | 11 | 7 |

Table 3. Dataset Characteristics of the proposal and Conventional Groups.

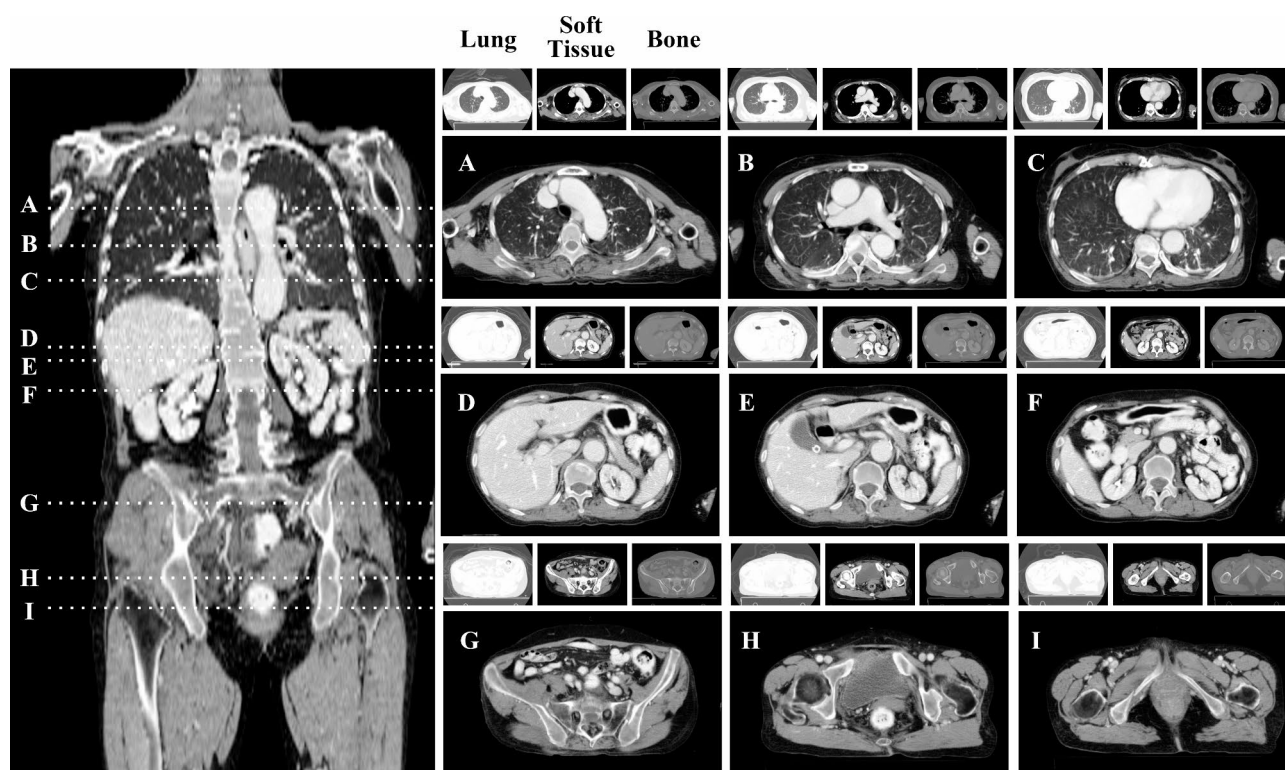


Fig. 2. A series of images produced by the Uni-CT Algorithm. These nine axial images were selected to highlight the effect of the Uni-CT Algorithm. Each proposal image has corresponding conventional lung, soft-tissue, and bone condition images.

parenchymal organs. The images of the pelvis (Fig. 2G, H, I) show optimized pelvic bones, intestines, bladder, and blood vessels, facilitating simultaneous detection of pelvic fractures, intra-abdominal bleeding, retroperitoneal hemorrhage, and organ injuries.

Representative axial images of the chest (A, B, C), abdomen (D, E, F), and pelvis (G, H, I) are displayed accordingly. Each proposal image has corresponding conventional images. The window settings of each conventional image are WW: 1500 and WL: -700 for the lung condition, WW: 350 and WL: 50 for the soft tissue condition, and WW: 2000 and WL: 200 for the bone condition.

Diagnostic agreement of physicians

The overall agreement rate among the four physicians regarding observed findings was $\kappa = 0.70$, with $\kappa = 0.70$ for the proposal group and $\kappa = 0.71$ for the conventional group, indicating substantial agreement.

Diagnostic accuracy of physicians in proposal and conventional groups

The average accuracy, sensitivity, and specificity of physicians in diagnosing target findings per patient were 84.8%, 74.3%, 96.9% for the proposal group and 85.5%, 81.3%, 91.5% for the conventional group, showing no significant difference (The result of the bayesian statistical analysis is in Supplementary Sect. 2). Table 4 details the accuracy, sensitivity, and specificity of each physician per patient and for each target finding.

Diagnostic speed of physicians in proposal and conventional groups

The average diagnostic speed per patient was 71.9 s for the proposal group and 110.4 s for the conventional group ($p < 0.05$), marking a 34.9% reduction in diagnosis time for the proposal group (The result of the bayesian statistical analysis is in Supplementary Sect. 2). The diagnostic speeds for each physician per patient in each group are presented in Table 4.

Discussion

This is the first study to propose and implement a Uni-CT algorithm to automatically generate a single series of total-body CT images by concatenating multiple images of segmented organs using organ-specific window settings. Our algorithm enables the simultaneous visualization of each organ in an optimal window setting in a single series of images without the necessity of alternating window settings. Previous research attempted to reduce the complexity of manual switching conditions by superimposing multiple window-setting images^{14–18}. Consequently, an ambiguously superimposed image loses the distinct characteristics of each window setting and fails to display an optimal image for each organ. In contrast, our algorithm extracted organ structures, applied organ-specific window settings, and concatenated them into a single series of images without superimposing multiple window settings. These concatenated images retained the distinct characteristics of each organ-specific window setting. In addition, particularly in emergency situations where lung, bone, and soft tissue conditions are typically observed with fixed window settings^{9–11}, our automated optimization for each organ may enhance comprehension compared to images cycled among fixed conditions for the lung, bone, and soft tissue. Thus, our approach streamlines diagnosis without the need to switch conditions and also enables the recognition of interrelations between image findings visible only under optimal conditions for each organ.

Furthermore, this study is the first to examine the effect of the Uni-CT algorithm on the accuracy and speed of diagnoses in total-body CT scans of trauma, quantitatively assessing the influence of this window setting on trauma CT diagnosis. These findings suggested that employing the multiple organ windowing algorithm in diagnosing total-body CT images for trauma can significantly reduce diagnosis time by 35% without compromising diagnostic accuracy. The algorithm was evaluated in trauma patients, necessitating comprehensive whole body organ assessment, especially when expediting diagnosis time is critical. The reduction in diagnosis time for trauma, which necessitates the evaluation of whole-body organs, suggests the potential to decrease diagnosis times for other internal diseases as well, potentially alleviating the workload of radiologists in routine image diagnostics.

In addition, leveraging this algorithm for the preprocessing of CT images for training can considerably enhance the accuracy of AI models. Previous imaging diagnosis models, often trained on images under a single

| | Proposal* | Conventional* |
|----------------------|------------------------------------|-----------------------------------|
| Physician 1 | | |
| Accuracy | 88.0 (95.0/90.0/100.0/90.0/65.0) | 90.0 (100.0/80.0/95.0/95.0/80.0) |
| Sensitivity | 78.3 (50.0/88.9/100.0/90.0/36.4) | 84.2 (100.0/78.9/66.7/95.0/57.1) |
| Specificity | 100.0 (100.0/100.0/100.0/NA/100.0) | 98.3 (100.0/100.0/100.0/NA/92.3) |
| Diagnostic speed (s) | 46.2 | 66.9 |
| Physician 2 | | |
| Accuracy | 87.0 (95.0/85.0/100.0/100.0/55.0) | 86.0 (100.0/75.0/90.0/85.0/80.0) |
| Sensitivity | 80.8 (50.0/83.3/100.0/100.0/36.4) | 77.5 (100.0/73.7/33.3/85.0/71.4) |
| Specificity | 95.8 (100.0/100.0/100.0/NA/77.8) | 95.8 (100.0/100.0/100.0/NA/84.6) |
| Diagnostic speed (s) | 57.1 | 96.5 |
| Physician 3 | | |
| Accuracy | 78.0 (90.00/90.0/100.0/50.0/60.0) | 81.0 (100.0/75.0/90.0/75.0/65.0) |
| Sensitivity | 56.7 (0.0/88.9/100.0/50.0/27.3) | 72.5 (100.0/73.7/33.3/75.0/57.1) |
| Specificity | 100.0 (100.0/100.0/100.0/NA/100.0) | 92.5 (100.0/100.0/100.0/NA/69.2) |
| Diagnostic speed (s) | 60.1 | 110.4 |
| Physician 4 | | |
| Accuracy | 86.0 (90.0/95.0/90.0/95.0/60.0) | 85.0 (90.0/85.0/65.0/100.0/85.0) |
| Sensitivity | 81.7 (0.0/94.4/0.0/95.0/54.5) | 90.8 (100.0/84.2/66.7/100.0/85.7) |
| Specificity | 91.7 (100.0/100.0/94.7/NA/66.7) | 79.2 (89.5/100.0/64.7/NA/84.6) |
| Diagnostic speed (s) | 124.1 | 167.6 |

Table 4. Details of Diagnostic Accuracy and Speed of Each Physician * Data in parentheses are Label A/Label B/Label C/Label D/Label E.

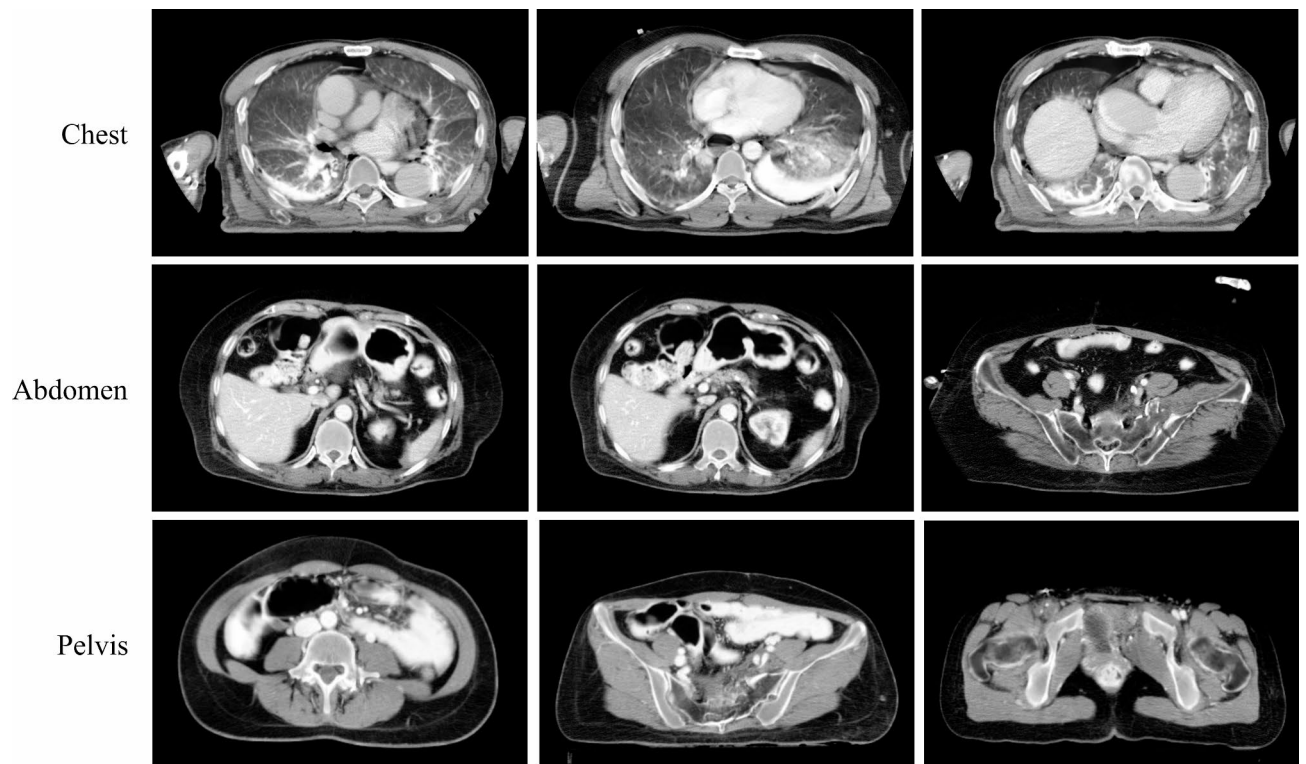


Fig. 3. CT images of typical blunt trauma injuries processed by the Uni-CT algorithm. The Uni-CT algorithm enables the simultaneous detection of multiple findings, revealing the direction and extent of the applied force.

condition^{28–32}, lacked representation of nontarget organs with appropriate windowing. Using this algorithm could expand training to include indirect findings among surrounding organs, thereby enhancing the learning scope and accuracy of the model.

Advantages of dynamic windowing

The algorithm developed in this study incorporates dynamic windowing, enabling the generation of optimal images under various conditions, including different CT equipment, viewer characteristics, and in the presence of artifacts. This flexibility in settings could also be applied to imaging various non-traumatic diseases.

Effect of Uni-CT algorithm on typical injuries

Blunt chest trauma often involves concurrent rib fractures, a pneumo/hemothorax, and extensive lung contusions. The algorithm enables simultaneous detection of these injuries, potentially increasing diagnostic speed and use of indirect signs such as fractures to diagnose pneumo/hemothorax or extensive lung contusions. Blunt abdominal trauma frequently presents as rib fractures, pneumo/hemothorax, lung contusions, and parenchymal organ injuries. The algorithm enables the simultaneous detection of these findings, revealing the direction and extent of the applied force in cases such as splenic and left renal injuries concurrent with left pelvic fractures. Blunt pelvic trauma often involves pelvic fractures, vertebral fractures, and retroperitoneal hematomas. This algorithm allows simultaneous detection of these injuries, aiding in identifying hematomas using indirect signs of fracture patterns (Fig. 3). Uni-CT applied total-body CT images of these cases are shown at the following URL: https://drive.google.com/drive/folders/126u5KOfM7hABtNW3s0XhGe3_8TtakSk?ths=true.

Limitations

In this study, we used image data from a single Japanese facility. The applicability of our algorithm remains unvalidated across different countries with varying ethnic groups, demographics, and CT equipment manufacturers. Further data collection and tuning of percentile scores under diverse conditions are necessary. When implementing the Uni-CT algorithm in a clinical setting, it is essential to consider its processing time. In this study, as noted in Sect. 2 of the appendix, output results can be obtained in tens of seconds even on a standard commercially available laptop GPU machine. It will be necessary to set up an environment with a higher-spec GPU machine to ensure faster output and a stress-free user experience feasible for clinical application. In the Uni-CT algorithm, anatomical structures were first extracted, and window settings were subsequently calculated for each structure. Therefore, the miss extractions lead to incorrect window settings calculations, resulting in incorrect output images. Enhancing semantic segmentation model accuracy for anatomical structure extraction is imperative. Cases with strong artifacts³³ were excluded, and the effectiveness of the algorithm in such cases remained untested. Future studies should consider cases with strong artifacts. The study focused only on patients

with blunt trauma, excluding the efficacy of the algorithm in penetrating trauma injuries. Further investigation is required in this area. The study used venous-phase CT images, and the evaluation of arterial-phase information was not possible. Future studies should consider incorporating different imaging phases. The study focused solely on verifying the findings necessitating urgent intervention, leaving the effectiveness of the algorithm for minor injuries unclear. Further trials with fewer severe cases are warranted.

Conclusion

To improve the efficiency of interpretation of total-body CT for trauma, we introduced a novel “unified CT image using an organ-specific windowing (Uni-CT)” algorithm. This enabled the diagnosis of critical findings in a single series of images. The algorithm suggests potential for significantly enhancing diagnostic speed for critical injuries in total-body CT for trauma without compromising the accuracy of physician diagnoses.

Data availability

Anonymized data will be available. The corresponding author will provide the data with respect to the data-sharing policy in the protocol and ethical approval of the study.

Received: 8 September 2024; Accepted: 13 December 2024

Published online: 15 February 2025

References

1. World Health Organization. Preventing Injuries and Violence: An Overview. (2022).
2. Rossier, N. D. Trauma—the forgotten pandemic? *Int. Orthop.* **46**, 3–11 (2022).
3. Toida, C. et al. Ten-year in-hospital mortality trends among Japanese injured patients by age, injury severity, injury mechanism, and injury region: A nationwide observational study. *PLoS One.* **17**, e0272573 (2022).
4. Huber-Wagner, S. et al. Effect of whole-body CT during trauma resuscitation on survival: a retrospective, multicentre study. *Lancet.* **373**, 1455–1461 (2009).
5. Hajibandeh, S. & Hajibandeh, S. Systematic review: effect of whole-body computed tomography on mortality in trauma patients. *J. Inj Violence Res.* **7**, 64–74 (2015).
6. Qamar, S. R. et al. Emergent Comprehensive Imaging of the Major Trauma Patient: A New Paradigm for Improved Clinical Decision-Making. *Can. Assoc. Radiol. J.* **72**, 293–310 (2021).
7. Fink, C., Alkadhi, H., Boll, D. T. & Johnson, T. Kachelrie, M. Advances in CT technology. *Invest. Radiol.* **45**, 289 (2010).
8. Geyer, L. L. et al. Incidence of delayed and missed diagnoses in whole-body multidetector CT in patients with multiple injuries after trauma. *Acta radiol.* **54**, 592–598 (2013).
9. Agostini, C. et al. Value of double reading of whole body CT in polytrauma patients. *J. Radiol.* **89**, 325–330 (2008).
10. Eurin, M. et al. Incidence and predictors of missed injuries in trauma patients in the initial hot report of whole-body CT scan. *Injury.* **43**, 73–77 (2012).
11. Ichinose, Y. et al. Time-oriented three-step evaluation of trauma pan-scan, starting with focused assessment with CT for trauma (FACT). *J. Jpn Assoc. Surg. Trauma.* **28**, 21–31 (2014).
12. Pomerantz, S. M. et al. Liver and bone window settings for soft-copy interpretation of chest and abdominal CT. *AJR Am. J. Roentgenol.* **174**, 311–314 (2000).
13. Patten, R. M., Gunberg, S. R., Brandenburger, D. K. & Richardson, M. L. CT detection of hepatic and splenic injuries: usefulness of liver window settings. *AJR Am. J. Roentgenol.* **175**, 1107–1110 (2000).
14. Mandell, J. C. et al. Clinical Applications of a CT Window Blending Algorithm: RADIO (Relative Attenuation-Dependent Image Overlay). *J. Digit. Imaging.* **30**, 358–368 (2017).
15. Anam, C., Budi, W. S., Haryanto, F., Fujibuchi, T. & Dougherty, G. A novel multiple-windows blending of CT images in red-green-blue (RGB) color space: Phantoms study. *Sci. Vis.* **11**, 56–69 (2019).
16. Mandell, J. C. & Khurana, B. Clinical applications of a computed tomography color marrow mapping algorithm to increase conspicuity of nondisplaced trabecular fractures. *Emerg. Radiol.* **26**, 59–66 (2019).
17. Snoeckx, A. et al. Lesion detection on a combined All-in-One window compared to conventional window settings in thoracic oncology chest CT examinations. *Diagn. Interv. Imaging.* **101**, 25–33 (2020).
18. Miskin, N., Caton, T., Guenette, M. Jr, Mandell, J. C. & J. P. & Computed tomography window blending in maxillofacial imaging. *Emerg. Radiol.* **27**, 57–62 (2020).
19. Yao, G. Value of window technique in diagnosis of the ground glass opacities in patients with non-small cell pulmonary cancer. *Oncol. Lett.* **12**, 3933–3935 (2016).
20. Fisher, S. R. A. & Yates, F. *Statistical Tables for Biological, Agricultural and Medical Research* (Hafner Publishing Company, 1953).
21. Wasserthal, J. et al. TotalSegmentator: Robust Segmentation of 104 Anatomic Structures in CT Images. *Radiol. Artif. Intell.* **5**, e230024 (2023).
22. Gilroy, A. M., MacPherson, B. R., Ross, L. M. & Broman, J. *Atlas of Anatomy* (Thieme Medical Pub, 2016).
23. Reshetov, A. Morphological antialiasing. in *Proceedings of the Conference on High Performance Graphics 2009* 109–116 Association for Computing Machinery, New York, NY, USA, (2009).
24. Seeram, E. Computed Tomography: Physical Principles and Recent Technical Advances. *J. Med. Imaging Radiat. Sci.* **41**, 87–109 (2010).
25. Romans, L. E. *Computed Tomography for Technologists: A Comprehensive Text* (Lippincott Williams & Wilkins, 2010).
26. Davies, M. & Fleiss, J. L. Measuring Agreement for Multinomial Data. *Biometrics.* **38**, 1047–1051 (1982).
27. Mishra, P., Singh, U., Pandey, C. M., Mishra, P. & Pandey, G. Application of student’s t-test, analysis of variance, and covariance. *Ann. Card Anaesth.* **22**, 407–411 (2019).
28. Masoudi, S. et al. Quick guide on radiology image pre-processing for deep learning applications in prostate cancer research. *J. Med. Imaging (Bellingham)*. **8**, 010901 (2021).
29. Lee, H., Kim, M. & Do, S. Practical Window Setting Optimization for Medical Image Deep Learning. Preprint at (2018). <https://arxiv.org/abs/1812.00572>
30. Zhang, K. et al. Clinically Applicable AI System for Accurate Diagnosis, Quantitative Measurements, and Prognosis of COVID-19 Pneumonia Using Computed Tomography. *Cell* **182**, 1360 (2020).
31. Wang, Z. et al. Detection and subtyping of hepatic echinococcosis from plain CT images with deep learning: a retrospective, multicentre study. *Lancet Digit. Health.* **5**, e754–e762 (2023).
32. Weston, A. D. et al. Automated Abdominal Segmentation of CT Scans for Body Composition Analysis Using Deep Learning. *Radiology.* **290**, 669–679 (2019).
33. Boas, F. E. & Fleischmann, D. CT artifacts: causes and reduction techniques. *Imaging Med.* **4**, 229–240 (2012).

Acknowledgements

We thank the radiologist team in Osaka General Medical Center for providing de-identified CT images from blunt trauma patients. We thank many volunteers for collecting radiology reports and medical records. We thank all of the volunteers for diagnostic imaging. We thank all of the medical staff in Osaka General Medical Center for their assistance and helpful discussions.

Author contributions

S.N collected the data. C.L. and S.M analyzed data. S.I. analyzed the data and constructed the models and software system. Y.M. supervised the statistics. N.O. conceived and supervised the project and wrote the manuscript with assistance from S.F., G.Y., and T.K. All authors discussed the results and reviewed the manuscript.

Funding

This study was conducted under the budget of the Japanese Agency for Medical Research and Development project (22he1022008h0001, 23he1022008h0002). The funders were not involved in the design of the study, its interpretation, or the writing of the paper. The corresponding author is responsible for all the work performed.

Declarations

Competing interests

Naoki Okada received grants from the Japanese Agency for Medical Research and Development project (22he1022008h0001, 23he1022008h0002). Naoki Okada and Shusuke Inoue are board members of fcuro inc. Other authors declare no conflict of interests.

Additional information

Supplementary Information The online version contains supplementary material available at <https://doi.org/10.1038/s41598-024-83346-y>.

Correspondence and requests for materials should be addressed to N.O.

Reprints and permissions information is available at www.nature.com/reprints.

Publisher's note Springer Nature remains neutral with regard to jurisdictional claims in published maps and institutional affiliations.

Open Access This article is licensed under a Creative Commons Attribution-NonCommercial-NoDerivatives 4.0 International License, which permits any non-commercial use, sharing, distribution and reproduction in any medium or format, as long as you give appropriate credit to the original author(s) and the source, provide a link to the Creative Commons licence, and indicate if you modified the licensed material. You do not have permission under this licence to share adapted material derived from this article or parts of it. The images or other third party material in this article are included in the article's Creative Commons licence, unless indicated otherwise in a credit line to the material. If material is not included in the article's Creative Commons licence and your intended use is not permitted by statutory regulation or exceeds the permitted use, you will need to obtain permission directly from the copyright holder. To view a copy of this licence, visit <http://creativecommons.org/licenses/by-nc-nd/4.0/>.

© The Author(s) 2025